Sustainable nanoporous gold with excellent SERS performances

Materials Chemistry and Physics 293 (2023) 126883

Sustainable nanoporous gold with excellent SERS performances

Deepti Raj [a], Mauro Palumbo [a], Gianluca Fiore [a], Federica Celegato [b], Federico Scaglione [a,*], Paola Rizzi [a]

[a] *Dipartimento di Chimica e Centro Interdipartimentale NIS (Nanostructured Surfaces and Interfaces), Universita` di Torino, Via Pietro Giuria 7, 10125, Torino, Italy*
[b] *Istituto Nazionale di Ricerca Metrologica (INRIM), Str. delle Cacce 91, 10135, Torino, Italy*

HIGHLIGHTS

- A low-cost Nanoporous Gold (NPG) was prepared by chemical dealloying of a $Au_{33}Fe_{67}$ supersaturated solid solution.
- $Au_{33}Fe_{67}$ ribbons were obtained by rapid solidification technique.
- Calphad calculations were done for a better knowledge of the thermodynamics of the Au–Fe system.
- Economic and sustainability factors have been discussed.
- NPG reveals excellent SERS activity with LOD of 10^{-15} M for 4,4′-bi-pyridine probe molecule.

Keywords:
Au-Fe
Nanoporous gold
Dealloying
SERS
Rapid solidification
CalPhad
Solidification process

ABSTRACT

A low-cost Nanoporous Gold (NPG) has been successfully produced by utilizing the simple method of chemical dealloying. Ribbons of a supersaturated solid solution $Au_{33}Fe_{67}$ were obtained by rapid solidification using melt-spinning technique. Chemical dealloying of the ribbons was achieved in 1 M HNO_3 at 70 °C for varying lengths of time. The as-quenched ribbon and as-dealloyed samples have been structurally and compositionally investigated using XRD, FESEM and EDS techniques. The obtained NPG is homogeneous with tunable ligament size and shape, easy-to-handle and free-standing. NPG has been successfully applied as substrate for Surface-Enhanced Raman Scattering (SERS) using 4,4′-bi-pyridine probe molecule. An impressive enhancement in the SERS effect has been observed. The detection limit is recorded to be as low as 10^{-15} M. The NPG sample shows great potential as an economical and highly sensitive SERS-active substrate for life science applications and ultrasensitive instrumentation. Catalytic properties have been explored demonstrating a high activity of the material. Most notably, a metastable precursor has been favourably obtained from an immiscible Au–Fe system. Usage of critical raw materials has been avoided. A cost-effective starting material has been used in the form of an Fe-rich precursor by pairing abundant and cheap Fe with Au. Then, an elegant and rapid dealloying procedure makes the overall production of NPG an inexpensive and sustainable process.

1. Introduction

Nanoporous (NP) metallic materials, an exceedingly interesting class of materials with unique physical and chemical properties, continue to be profoundly useful in fields of catalysis, hydrogen storage, molecular sieves, fuel cells etc. [1]. An NP metal has a morphology constituted by ligaments and pores in a three-dimensional framework of a nearly pure metal [1]. Nanoporous gold (NPG) is one of the most favourable NP metals with a number of applications such as in electrocatalysis [2], SERS [3], as sensors [2] etc. ascribed to its peculiar properties, i.e., extraordinary catalytic activity, large surface area and free-standing samples [4].

A technique which has gained substantial fascination for tailoring NP metals is dealloying - a phenomenon of corrosion involving the removal of the less noble metal from a solid solution alloy selectively [5]. During this process, Au ad-atoms rearrange simultaneously by surface diffusion forming a network of ligaments and open pores [6–8]. Dealloying can be used for both crystalline and amorphous alloys [9,10]. The state of the chosen alloy precursor determines the morphology of the obtained NP metal [4,11]. In case of dealloying a crystalline alloy, the parent

https://doi.org/10.1016/j.matchemphys.2022.126883

microstructure is retained and a single porous crystal evolves from each grain [12], contrary to the case of amorphous precursors in which ligaments result from the impingement of numerous fine crystals [4,13,14]. There are several types of dealloying among which chemical and electrochemical are the most performed. One of the most important parameters governing the process of chemical dealloying is the parting limit defined as the minimum value of the more noble metal's concentration in the solid solution alloy above which dealloying will not occur [1,15,16]. The NP metal obtained by dealloying can be customized for specific uses in terms of ligament and pore size and shape which is easily done by altering the trial conditions, i.e., extent of dealloying treatment, electrolyte's type, concentration and pH, and temperature of dealloying and precursor [17].

In this study, the choice of metal to be paired with Au was largely dependent on: (i) mechanical strength; (ii) cheap and abundant availability; and (iii) the ease of dealloying in attainable experimental conditions using common electrolytes. Iron satisfies all of the above-mentioned criteria. The composition for the master alloy was opted to be Fe-rich so as to minimize the amount of expensive Au, yet keeping it within the parting limit. After a careful analysis of the equilibrium phase diagram of the Au–Fe system, the minimum possible Au composition which can be used for successful dealloying was determined to be 33 at. % Au. The phase diagram clearly displays extended miscibility gap of these metals in the solid state [18] due to the contrast in the structures of the body-centred cubic (bcc) Fe and face-centred cubic (fcc) Au as well as in their lattice parameters [19]. There is absence of any intermetallic compound. Although Fe and Au have no solubility in each other at room temperatures [19], by rapid solidification the elements can be forced to form a supersaturated solid solution which is stable at room temperature [20–22].

The most active metal used in HER is Pt. But it comes with its drawbacks, i.e., costliness, limited availability and inadequate durability [23]. Efforts to fabricate and develop an efficient and durable non-Pt catalysts with comparable catalytic activity have been at the forefront in recent years because of the incessant worldwide energy demands [24]. Reported is the use of palladium nanocubes coated with molybdenum [25]; nanoparticles of Au–Ni alloy supported on reduced graphene oxide [26]; gold aerogel supported on graphite carbon nitrite [27]; N, P co-doped carbon nanofiber networks [28]; M_3C (M: Fe, Co, Ni) nanocrystals encased in nanoribbons of graphene [29] nanoparticles of Pd–Ru encapsulated in porous carbon nanosheets [30]; CoP nanocrystals that are urchin-like [31]; Phosphorus doped MoS_2 [32]; nanostructured porous gold film [33]; anodized NPG [34]; and amorphous MoS_2 on NPG [4] among many others as alternative materials to Pt. NP metals are of significant interest in this respect. In the same thread, considering their large surface area, nobility and inexpensiveness, we examined the HER activity of one of the obtained NPG samples.

Surface-Enhanced Raman Scattering (SERS) is an outstanding trace-level molecular detection technique in biological and chemical systems owed to its remarkable molecular sensitivity and specificity [3,35]. A combined effect of chemical [36] and electromagnetic enhancements [37] has been recognized as the cause of the strong SERS amplification. Species chemisorbed to the surface form a charge-transfer complex which generates the chemical effect [38] while the resonant coupling between the incident laser light and localized surface plasmons give rise to the electromagnetic effect [38,39] at nanopores, sharp edges and tips called "hot spots" [40,41]. Numerous evidences have been reported regarding successful utilization of NPG as a SERS substrate as they offer countless active sites augmenting the excitations of localized surface plasmons [41–44]. Thus, one of the produced NPG samples obtained from a simple synthetic procedure has been tested as a highly active, steady and inexpensive alternative to previously reported NPG samples.

In this paper, NPG has been fabricated from $Au_{33}Fe_{67}$ supersaturated solid solution precursor of composition 67 at. % Fe and 33 at. % Au within the parting limit of Au. Chemical dealloying has been accomplished in 1 M HNO_3 at 70 °C for diverse durations. HER and SERS studies have been reported utilizing the enhanced surface area and typically numerous active sites offered by the NPG sample. The sample has displayed excellent performance as discussed in detail below. The important factors of affordability and sustainability of the proposed nanoporous metal have also been discussed which make it a competitive candidate among contemporary commercial materials.

2. Experimental

To prepare the $Au_{33}Fe_{67}$ master alloy with target composition of 67 at. % Fe and 33 at. % Au, pure elements (99.95% Fe and 99.99% Au) were subjected to arc-melting in Ti-gettered Ar atmosphere. Rapidly solidification of the obtained ingot was achieved by melt-spinning technique at a linear speed of 25 m s^{-1} in a closed chamber under Ar atmosphere. The obtained ribbons were long, continuous and homogeneous having 15 μm thickness and 8 mm width.

Dealloying of the as-quenched $Au_{33}Fe_{67}$ ribbon was performed chemically in 1 M HNO_3, at 70 °C, for durations of various lengths ranging from 1 h to 48 h. Chemical grade reagents and deionized water were used to prepare all electrolytes. Samples were rinsed in deionized water, air-dried and stored in a closed and clean box before characterization.

Characterization techniques involved Panalytical X-pert X-ray Diffractometer in Bragg–Brentano geometry for phase determination, the obtained XRD patterns were analysed using the Xpert Highscore software and peak assignments were done utilizing the ICDD database provided by the software. Moreover, Field-Emission Scanning Electron Microscopy and Energy Dispersive X-ray Spectroscopy were used for morphological and compositional analyses respectively.

The HER activity of the obtained NPG was evaluated at room temperature in 0.5 M H_2SO_4. Three-electrode cell configuration was used, i.e., NPG sample as the working electrode, Pt-grid counter-electrode and saturated Ag/AgCl double-bridge reference electrode. Linear Sweep Voltammetry (LSV) was conducted in 0.5 M H_2SO_4 from 0.54 V to −0.39 V vs RHE at 2 mV s^{-1} scan speed. As reference, a pure Pt sheet was used. All potentials were reported to the reversible hydrogen electrode (RHE) adding a value of (0.199 + 0.059 × pH) V. Electrochemically Active Surface Area (EASA) for the selected NPG sample was estimated by electrochemical oxidation of 0.5 M KOH via Cyclic Voltammetry (CV) at a 20 mV s^{-1} scan rate from 0.4 V to 1.6 V vs RHE [45,46] (Fig. S3 in the supplementary material). The area under the reduction peak of the graph collected from the CV reveals the EASA by providing an account of the electrochemically active sites [47] which came out to be 6.48 cm^2. The obtained EASA was used in normalizing the current density.

SERS measurements were conducted by a Renishaw inVia Raman Microscope with 785 nm laser line (0.05% power, 50 × ULWD objective, acquisition time of 20 s); the SERS probe molecule was chosen to be 4,4′-bipyridine (bipy) [35]. Firstly, concentrated HNO_3 was used to clean the NPG sample for 5 min, followed by rinsing with de-ionized water. Afterwards, the ethanol solution of bipy of 10^{-9} M, 10^{-12} M and 10^{-15} M concentrations were used to immerse the sample for 20 min, which enabled adsorption of the probe molecules on the sample surface. Diluted solutions were freshly prepared the day before the experiments and stored in new wide neck 50 ml PE bottles. The volume of solution used for adsorption is that one of an Eppendorf vial of 1 ml. This amount of solution was taken from the PE bottle using a 1000 μl mechanical micropipette, taking care of using a new tip per each concentration. Therefore, no contamination is expected. After air-drying, the sample surface was measured.

This protocol was followed for the SERS experiments: the same piece of sample was used for all the measurements at different bipy concentrations, starting from the lowest concentration of 10^{-16} M. The sample did not show any signals. Then, the sample was washed and immersed it in a higher concentration of 10^{-15} M for 20 min. This time the sample showed good signals at 5 different sites establishing the fact that 10^{-15} M was the limit of detection. Afterwards, the same procedure of

washing, immersing and measuring the sample was repeated in higher concentrations until 10^{-9} M.

Based on the representative peak at 1614 cm^{-1} SERS intensity mapping image was collected in a 20 × 30 μm^2 area with step size of 5 μm, a spot size of 2 × 1 μm^2 and 35 points for 10^{-12} M bipy concentration. Chemical grade reagents and de-ionized water were used to prepare all solutions.

The Calphad method was applied to perform thermodynamic calculations [48] using the ThermoCalc software v. 2021a [49]. Literature was referred for the thermodynamic parameters for the Au–Fe system [50].

3. Results and discussion

3.1. Microstructures obtained from rapid solidification

Fig. 1 depicts the SEM back-scattered electron (SEM-BSE) image of the as-quenched ribbon cross-section (Fig. 1 (a)) together with a magnified image of the air-side (Fig. 1 (b)) and wheel-side (Fig. 1 (c)) surface of the ribbons. At a first glance, the wheel-side area appears to be constituted by a finer microstructure, while the air-side shows a coarser microstructure with a quite well-defined line of microstructure change visible in the middle of the ribbon cross section (Fig. 1 (a)). This is mainly due to the faster quenching rate during the process of solidification acting over the side of the ribbon that lies in direct contact with the wheel. On the other hand, the air-side experiences a much lower and less efficient rate of heat extraction from the liquid melt [51]. At a more precise analysis it is possible to see that in the wheel side only a matrix with embedded precipitates can be observed, as displayed in Fig. 1 (b), while in Fig. 1 (c) the air-side is observably composed of dark dendritic grains and a bright matrix by with embedded precipitates.

In order to have a profound understanding of the microstructure of the rapidly solidified ribbon, Calphad calculations were done for a better knowledge of the thermodynamics of the Au–Fe system. In Fig. 2 (a) the calculated Au–Fe phase diagram is reported together with the metastable miscibility gap (green curve) in the fcc phase, originating two composition sets, one Au-rich and the other γ-Fe-rich. Furthermore, the T_0 lines for fcc (red curve) and bcc (blue curve) phases are also reported in the same figure. The T_0 lines are the locus of points (temperatures as a function of composition) where the Gibbs free energy of the liquid and a solid phase are equal [52]. As it can be seen, the T_0 line of fcc phase for the $Au_{33}Fe_{67}$ composition lies at 1183 °C, i.e., just 79 °C below the liquidus temperature and slightly higher than the peritectic temperature, so at undercoolings that can be easily achieved with quenching rates of with a melt-spinning apparatus. On the contrary, the T_0 line for the formation of a bcc phase lies at far lower temperatures. Therefore, we can expect that the liquid phase, reaching the T_0 line on cooling, is partition-less transformed into a fcc solid solution with $Au_{33}Fe_{67}$ composition. This conclusion can be further supported by the driving forces for nucleation estimated for pure Fe in both fcc and bcc structures and $Au_{33}Fe_{67}$ solid solutions in bcc and fcc structures from the liquid phase, as reported in Fig. 2 (b). It is possible to see that at elevated temperatures the fcc solid solution has a slightly greater driving force for nucleation from the liquid with respect to the other phases (inset in Fig. 2 (b)), while at lower temperatures (around 850 °C) the bcc solid solution gains a higher driving force for the formation during solidification.

On this basis, the microstructure of each side of the ribbon can be interpreted as follows:

i) **wheel side (**Fig. 1 **(b)):** An fcc (Au) solid solution with $Au_{33}Fe_{67}$ composition is formed directly from the liquid during the solidification with a partition-less solidification. This can be allowed by a significant undercooling of the liquid alloy due to the rapid solidification. T_0 curve lies close to the liquidus line so a limited undercooling is sufficient to allow the partition-less solidification of the

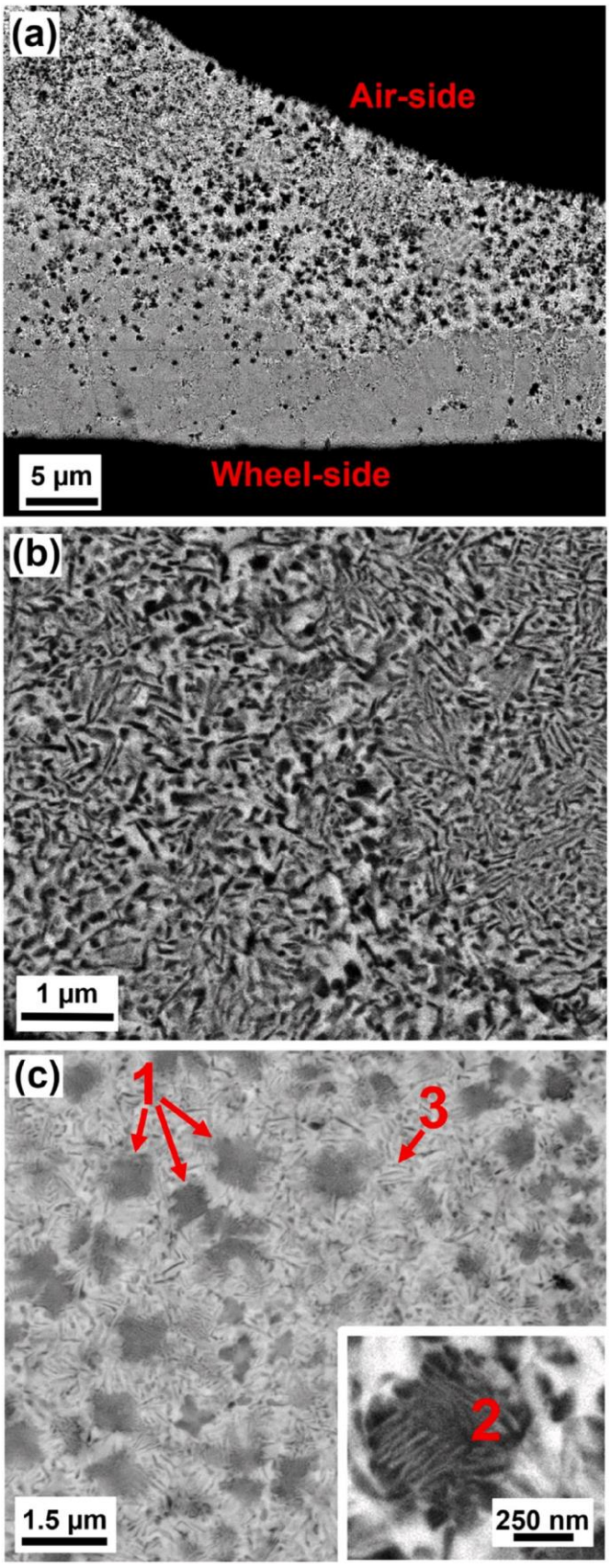

Fig. 1. SEM-BSE image of the as-quenched $Au_{33}Fe_{67}$ ribbon (a) cross-section; (b) wheel side surface; and (c) air side surface with the inset showing the magnification of the dendritic region with white lamellas.

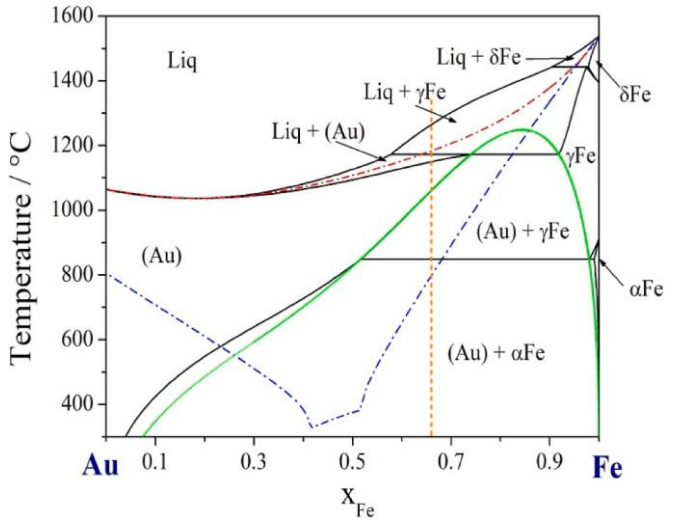

Fig. 2a. Au–Fe phase diagram (black curves) calculated using CALPHAD method. Green curve: fcc miscibility gap; T_0 line for the formation of a fcc phase (red curve) and bcc phase (blue curve). In orange is depicted the $Au_{33}Fe_{67}$ composition. (For interpretation of the references to colour in this figure legend, the reader is referred to the Web version of this article.)

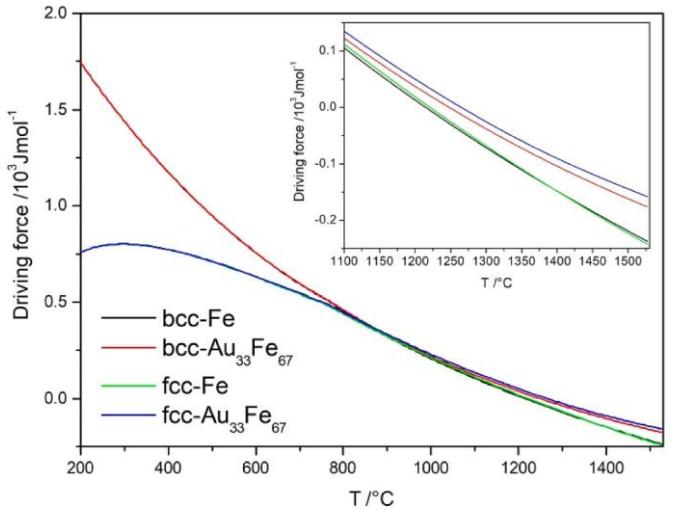

Fig. 2b. Driving forces for nucleation of pure Fe and $Au_{33}Fe_{67}$ solid solutions in both fcc and bcc structures from the liquid phase. Inset the order of 10^6 K/s, i.e., those obtained during rapid solidification shows a magnification of the driving force curves for temperatures above 1100◦C.

liquid with subsequent suppression of the peritectic reaction. During further cooling down, the metastable miscibility gap of the two fcc phases is reached and a consequent precipitation of a γ(Fe) phase can be expected from the fcc (Au) followed by the eutectoid reaction of the latter phase that mainly allows the change in structure of the fcc γ(Fe) into bcc α(Fe) with the formation of a limited amount of fcc (Au) with a eutectoidic microstructure (i.e., alternated lamellas of the two phases). At further cooling, from the fcc (Au) matrix, α(Fe) precipitates are formed (due to the large change in solubility of Fe in Au), while the already formed α(Fe) remains almost unchanged due to the small change in solubility of Au in Fe. So, to summarize, at the end of the solidification process, an fcc (Au) matrix can be observed (white phase in Fig. 1 (b)) with precipitates of bcc α(Fe) of different sizes depending on the temperatures at which they are formed during cooling (black precipitates in Fig. 1 (b)); moreover, alternated lamellas of the two phases must be present but these are difficult to be identified because of the large amount of alternated black and white grains.

ii) **air-side (**Fig. 1 **(c)):** The quenching rate is not rapid enough to allow the liquid to reach T_0 line in undercooling, therefore solidification from the liquid of the fcc γ(Fe) primary phase in dendritic shape can be expected. When the peritectic reaction occurs (at peritectic temperature or below) an fcc (Au) phase is formed due to the diffusion of Au atoms, present in the Au-rich liquid, into the fcc γ(Fe) dendrites. The diffusion coefficient of Au in Fe is low [51]. So, we can expect that at the acting solidification rates, the peritectic reaction is incomplete and the core of the former dendrites remains rich in Fe, i. e., fcc γ(Fe), while on the outer part of the pristine dendrites fcc (Au) is formed. When the solidification is completed below the solidus line the microstructure is therefore composed by two phases: i) fcc (Au) (the majority) and fcc γ(Fe) in small amount maintaining the original dendritic shape. During cooling down, the miscibility gap is reached so that fcc γ(Fe) precipitates are formed into the fcc (Au) phase. The eutectoid reaction allows the formation of a lamella like microstructure with the formation of alternating grains of fcc (Au) and bcc α(Fe); this microstructure is visible where the dendritic regions named 1 in Fig. 1 (c) are present in which white lamellas are visible. In the inset of Fig. 1 (c) a magnification of the dendritic regions is reported in which the eutectoid microstructure is evident (number 2 in inset of Fig. 1 (c)). Cooling down further to room temperature, the formation of bcc α(Fe) precipitates is observed in fcc (Au) visible in bright regions as darker acicular structures (number 3 in Fig. 1 (c)). This is due to the large slope of the solvus line and the large difference in solid solubility of Fe in Au at decreasing temperatures.

EDS analysis confirmed that the desired average composition of 33 at. % Au and 67 at. % Fe was obtained.

The as-quenched ribbon was characterized on both sides by XRD and no significant preferred orientation was detected in the patterns, while the phases described in the microstructure of the ribbons are confirmed. Fig. 3 (a) shows the XRD pattern of the as-quenched ribbon in which the peaks are present related to the solid solutions of bcc α(Fe) and fcc (Au), metastable and supersaturated, denoted by the orange dots and the green squares respectively. The peaks have been assigned considering the ICDD Au reference pattern 03-065-8601 and Fe reference pattern 03-065-4899. It is common knowledge that the lattice parameter of solid solutions can change depending on the composition. In this case, fcc (Au) phase has a lower lattice parameter with respect to pure Gold since Fe atoms have been incorporated in the Au structure and because of this

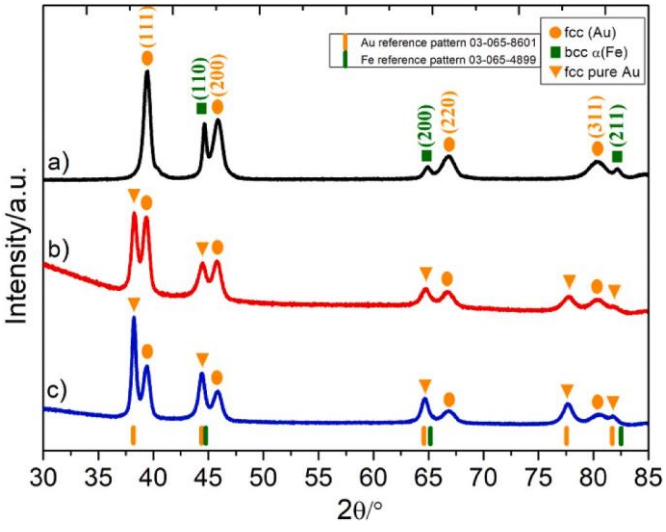

Fig. 3. XRD patterns of (a) the as-quenched ribbon, (b) NPG_1h and (c) NPG_8h.

the peaks in the XRD pattern are shifted towards higher diffraction angles [53]. This shift in the (Au) peaks can be easily noticed in the XRD pattern for the as-quenched ribbon. Similarly, the bcc α(Fe) solid solution sees an increase of the lattice parameter to accommodate Au atoms in the Fe lattice resulting in the shift of the Fe characteristic peaks towards smaller diffraction angles. This is corroborated by the Au and Fe lattice parameters in the as-quenched ribbon, i.e., 0.399 nm and 0.294 nm respectively.

3.2. Chemical dealloying

HNO_3 is a well-known and efficient electrolyte to remove Fe present in the alloy matrix simultaneously having no effect on the Au concentration. Chemical dealloying of the as-quenched ribbon was performed in 1 M HNO_3 at 70 °C for 1 h (NPG_1h), 2 h (NPG_2h), 4 h (NPG_4h), 6 h (NPG_6h) and 8 h (NPG_8h). Fig. 3 (b) shows the XRD pattern for NPG_1h. It can be noted that after 1 h of the dealloying treatment the peaks of bcc α(Fe) phase have disappeared from the pattern signifying the complete removal of the less noble phase from the alloy microstructure due to a galvanic effect. Moreover, the removal of Fe from the (Au) solid solution with a proper dealloying mechanism is also acting, probably starting when the bcc α(Fe) phase is completely dissolved into the electrolyte. The Fe removal enables the formation of Au-rich ligaments by surface diffusion of the Au adatoms on the surface of the pristine (Au) solid solution. This is observable in the XRD pattern due to the presence of emerging peaks of a new fcc phase, denoted by orange triangles, whose lattice parameter approaches that of pure Au. Given the smaller duration of dealloying, the pristine fcc (Au) phase can be clearly detected in the XRD pattern meaning that the sample has not been fully dealloyed. A rough estimation of the lattice parameter gave the value of 0.396 nm confirming the presence of the Au-rich fcc (Au) pristine phase, for which a similar a_0 was determined. This result is related to the limited change in the amount of Fe in the fcc (Au) phase, that remains almost unaffected in the core of the ligaments underneath the Au-rich layer produced by Au ad-atoms surface diffusion. For NPG_8h, the XRD pattern in Fig. 3 (c) shows that the amount of fcc (Au) solid solution is decreased with respect to the previous sample while the amount of almost pure Au phase is increasing, in fact, the (Au) solid

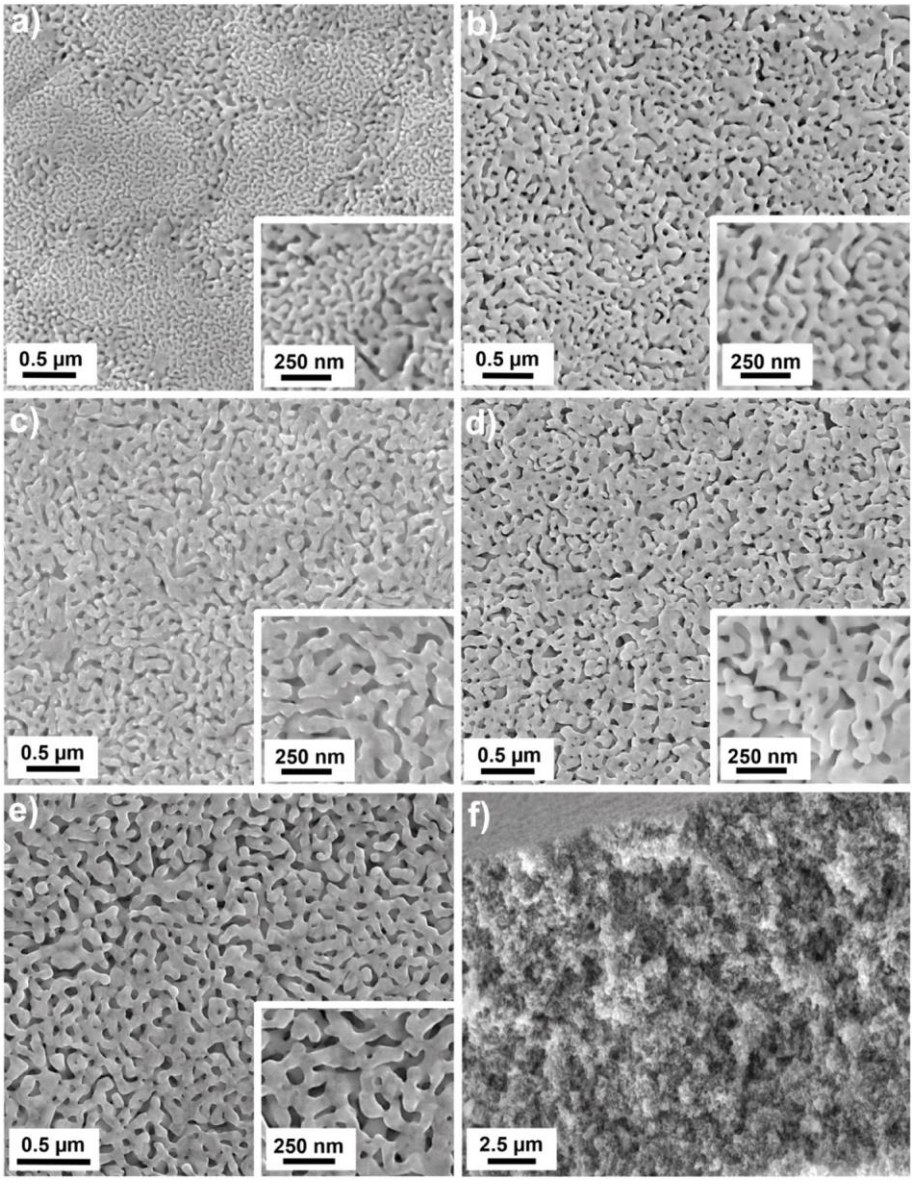

Fig. 4. SEM−SE images of (a) NPG_1h; (b) NPG_2h; (c) NPG_4h; and (d) NPG_6h; (e) NPG_8h; and (f) cross-section of NPG_8h. The insets show magnified view of respective samples.

solution peaks are reduced in intensity with respect to the NPG_1h sample, while the pure Au peaks are increased in intensity. This, obviously, means that more Au-rich ligaments have been formed as a result of longer duration of the dealloying treatment. Moreover, the amount of Fe in solid solution in Au ligaments is slightly reduced after 8 h of dealloying as a limited shift of the (Au) peaks is observed in NPG_8h with respect to NPG_1h. Interestingly, the fcc (Au) phase is present even after 8 h of the treatment revealing that a certain amount of Fe still exists in this phase which is not dealloyed.

The SEM secondary electron (SEM−SE) images are presented in Fig. 4 for the as-dealloyed samples. The sample NPG_1h (Fig. 4 (a)) exhibits a bimodal bicontinuous nanoporous morphology extended throughout the surface. There are small regions comprised of fine ligaments (approximately 29 nm) and surrounded by regions with comparatively bigger ligaments (approximately 52 nm). This bimodal morphology seems to be a result of variation of content distribution of Au and Fe in the as-quenched ribbon. The finer morphology must have originated from the dark dendritic grains of bcc α(Fe) phase as already shown in Fig. 1 (c), while the coarser one from the surrounding area rich in fcc (Au) phase. During dealloying, Fe was removed from both the phases but the presence of relatively higher Au content in the surrounding region resulted in slower rate of dealloying and faster surface diffusion of the Au atoms leading to formation of thicker and bigger ligaments. In addition, due to higher Fe content in the dark dendritic grains the dealloying rate is high leading to formation of finer ligaments. With an increase in the duration of the dealloying treatment, e.g., in NPG_2h, this morphological distinction tends to fade out slightly. This effect augments on increasing the dealloying time further as it allows the ligaments to diffuse into neighbouring regions coalescing and homogenizing the overall morphology. Eventually, the surface becomes more homogeneous and ligament sizes are in unison, i.e., 43 nm (Fig. 4 (e)). Moreover, coarsening is also observed at the same time during the process because of increased dealloying time as a consequence of which slight coverage of the nanopores can be noticed. Cross-sectional SEM images of NPG_1h, NPG_2h, NPG_4h and NPG_6h_have been provided in Fig. S1 while the side-by-side SEM−SE and BSE images of NPG_1h and NPG_8h can be found in Fig. S2 of the supplementary material. The EDS analysis gives the Au and Fe composition of each sample as follows: 65 at. % Au and 35 at. % Fe for NPG_1h; 71 at. % Au and 29 at. % Fe for NPG_2h; 81 at. % Au and 19 at. % Fe for NPG_4h; 88 at. % Au and 12 at. % Fe for NPG_6h; and 92 at. % Au and 8 at. % Fe for NPG_8h. To summarize, as the dealloying time increases, a surge is noticed in - (i) the atomic percentage of Au; (ii) the size of the ligament; (iii) the homogeneity of the surface morphology.

3.3. *Hydrogen evolution reaction studies*

The sample used for HER experiments was NPG_8h as, when compared to the other samples, it has the largest specific surface area evidenced by the CV measurements provided in Fig. S4 of the supplementary material. Since the active sites on the catalyst surface usually increase in number with increasing surface area, NPG_8h has the most number of active sites potentially generating the highest catalytic activity [54]. In addition, it possesses a homogeneous nanoporous morphology with the highest Au content, i.e., 92 at. %.

Fig. 5 (a) depicts the obtained HER polarization curves. −5 mA cm^{-2} current density is shown by the sample at −0.38 V overpotential. As evident from Fig. 5 (b) below, the obtained onset potential is −4 mV which is better than that for a bare Pt sheet, i.e., −13 mV. On comparison it is clear that the obtained onset potential is superior to numerous already reported electrocatalysts: −48 mV for nanostructured porous gold film (NPGF) [33]; −53.8 mV for self-supported Ni_3S_2 film on a nanoporous copper (Ni_3S_2@NPC) electrode [55]; 59 mV for Co, N-co-doped nanotube/graphene 1D/2D heterostructure (Co/NCNT/NG) [56]; −85 mV for bio-derived nanoporous activated carbon sheets [57]; 142 mV for MoS_2 nanosheets on 3D conductive MoO_2 (3D MoS_2/MoO_2)

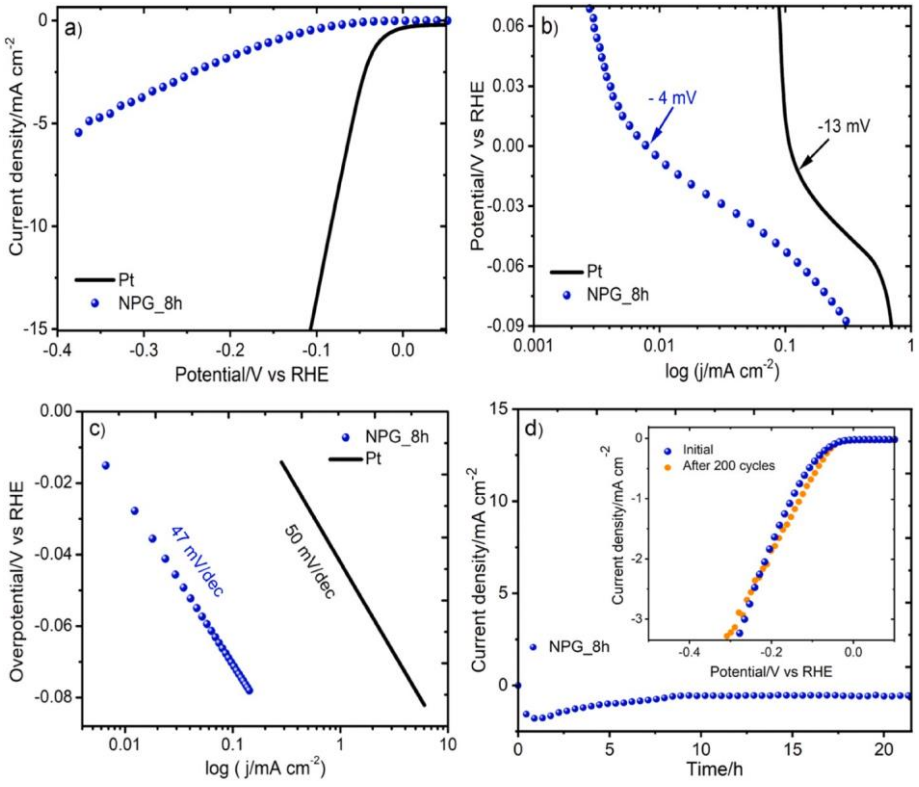

Fig. 5. (a) LSV polarization curves, (b) Onset potentials and (c) Tafel slopes for pure Pt (black solid line) and NPG_8h (blue spheres) (d) Chronoamperometric measurement for NPG_8h and inset shows the polarization curves of LSV for NPG_8h after potential-scanning for 200 cycles. (For interpretation of the references to colour in this figure legend, the reader is referred to the Web version of this article.)

[58]; and −164 mV for WS_2/PEDOT composites electrodeposited onto nanoporous gold [59].

The plot of overpotential vs log of current density in the region after the onset potential was used to estimate the Tafel plot of the sample and references. The Tafel equation below was used to linear-fit the data,

$$\eta = b \log j + a$$

η being overpotential, j, current density and b, Tafel slope.

The HER mechanism is determined by the Tafel slope based on the classical hydrogen evolution theory. Three key steps occur in an acidic environment: (i) the discharge or Volmer reaction, (ii) the combination or Tafel reaction and (iii) the desorption or Heyrovsky reaction [60,61]. In the first step discharge process comes into play involving interaction between a proton and an electron leading to formation of an adsorbed hydrogen atom on the surface of the electrode. If the reaction follows the Tafel step, H_2 is evolved from combination of two adsorbed hydrogen atoms, whereas in Heyrovsky, H_2 is generated when another electron combines with a proton and an adsorbed hydrogen atom. The Tafel slope also denotes the rate determining step (r.d.s.): 120 mV dec^{-1} or higher value - Volmer reaction; 40 mV dec^{-1} - Heyrovsky reaction while slopes close to 30 mV dec^{-1} - Tafel reaction [62]. From Fig. 5 (c), the Tafel slope for NPG_8h is determined to be 47 mV dec^{-1} which is much lower than that for Pt, i.e., 50 mV dec^{-1}. This signifies that a huge increment in the current density is achieved with a minor raise in the overpotential. The rate-determining step in this case should be the Heyrovsky reaction. The obtained Tafel slope value of 47 mV dec^{-1} proves to be better than quite a number of electrocatalysts such as 51 mV dec^{-1} for nanoporous ruthenium (np-Ru) [63]; 53 mV dec^{-1} for WS_2/PEDOT [59]; 54 mV dec^{-1} for MoP/N,P-rGO [64]; 63.5 mV dec^{-1} for Ni3S2@NPC [55]; 67 mV dec^{-1} for Co/NCNT/NG [56]; 74 mV dec^{-1} for nanoporous gold/-tungsten sulfide composite film [65]; and 85 mV dec^{-1} for NACS [57]. The intercept of the Tafel plot gives a large value of exchange current density, i.e., 0.12 mA cm^{-2} which indicates generation of high current at a given overpotential [66]. This also points towards high activity of the electrode surface, meaning the energy barrier is much lower allowing the charge to easily overcome it and move between the catalyst surface and the electrolyte which results in faster electrochemical reactions [66]. The obtained exchange current density, i.e., 0.12 mA cm^{-2}, is comparable to 0.126 mA cm^{-2} achieved in case of NPGF [33] while exceeding the value of 8.32×10^{-9} mA cm^{-2} for Au-MWCCE [67]; 5.9×10^{-5} mA cm^{-2} for nanoparticles of $CoTe_2$ [68]; and 9.0×10^{-4} mA cm^{-2} for 3D MoS_2/MoO_2 [58]; 0.04 mA cm^{-2} for WS_2/PEDOT [59]; 9.2×10^{-4} mA cm^{-2} for MoS_2–Mo-1h [69]; 1.92×10^{-3} mA cm^{-2} for CoNi@N–C/rGO [70]; 0.017 mA cm^{-2} for hierarchical nanotubes of β-Mo_2C [71]; and 0.017 mA cm^{-2} reported for carbon fibre Pd-modified electrode [72,73].

The stability of the electrocatalyst has been also evaluated. Chronoamperometric measurement was executed in 0.5 M H_2SO_4 at a potential of −0.18 V vs RHE as shown in Fig. 5 (d). The current remains remarkably stable for more than 20 h. In addition, LSV polarization curves were obtained for NPG_8h at a scan rate of 2 mV s^{-1} for 200 cycles of potential scans as depicted in the inset of Fig. 5 (d). The electrolyte colour or the electrode surface morphology suffered no visible change during the course or at the end of the measurements.

The brilliant catalytic performance of the NPG sample is ascribed to the innumerable active sites present in the sample by virtue of its nanoporous morphology, structure and composition. The structural defects combined with Au sites such as steps, edges or kinks that are lowly coordinated, act as active sites within the porous scaffold of the NPG sample [74]. The nanoporous geometry causes the reactant species to be trapped during the reaction displaying a nano-confinement phenomenon [75]. The numerous collisions between the trapped species and the active sites result in enhancement of the overall reaction efficiency [75]. Besides, the residual atoms of Fe, being a catalytically active metal itself, present in the NPG sample, also contribute to the defect sites thereby elevating the sample's total electrocatalytic proficiency [75,76].

Overall, based on these outstanding findings NPG_8h exhibits quite promising potential to be an electrocatalyst for HER. Since a simple, fast and cost-effective dealloying procedure has been used to obtain NPG_8h from a low-cost precursor, it can serve as a favourable alternative to Pt.

3.4. SERS studies

Noble metal based nanomaterials have been known to display powerful SERS enhancement credited to their exceptional surface plasmon resonance properties [77]. In the same thread, we tested NPG_8h for its performance as a SERS-active substrate owing to its homogeneous nanoporous morphology, highest Au-rich composition as well as the largest EASA. The sample was immersed for 20 min in ethanol solution of 4,4′-bipyridine (bipy) probe with diverse concentrations, i.e., 10^{-9} M, 10^{-12} M and 10^{-15} M bipy, after which the SERS effect was tested. The time of 20 min was chosen in accordance with our prior experience and thinking of a practical and routine application of the substrate; indeed, that time is enough to enable adsorption of the probe molecules on the sample surface and get a good signal.

Notably, the main objective of this SERS investigation was to estimate the low detection limit (LOD) of the NPG sample. Before and after the treatment, the sample was free-standing, bendable and easily handled with tweezers showing favourable characteristics for an active SERS-substrate. After 20 min of immersion in 10^{-15} M bipy solution SERS spectra on both surfaces of the sample were obtained after exciting by a 785 nm laser at five arbitrarily selected sites on each side as shown in Fig. 6 (a). At 1614, 1297, 1233, 1077 and 1026 cm^{-1} the characteristic peaks can be detected, fairly agreeing with the literature [35]. The spectra show a discrepancy in terms of the bandwidth and relative intensity at different sites which is caused by the adsorption kinetics and orientation of molecules along with the electromagnetic field disparity at each ''hotspot" [40]. These spectra that are similar in nature, allow us to predict that whatever the site on the sample surface the same type of spectrum will be obtained on an average; this is a good check of the readability of the SERS signal displayed by the NPG sample.

Fig. S5 (a) and (b) in the supplementary material show the SERS spectra obtained for 10^{-9} M and 10^{-12} M bipy solution using a 785 nm laser at five arbitrarily selected sites. The well-established electromagnetic mechanism serves as the primary reason for the observed enhancement of SERS effect on NPG which is related to effective surface plasmon excitation and confinement [78]. A bonus effect of localization of electromagnetic field in the pores is also in play [79]. The unique bi-continuous pore-ligament framework of the NPG sample with highly curved morphology offers highly dense low coordination sites such as holes, steps and kinks which interact strongly with the target molecules [74]. This allows for a conducive generation of local Raman ''hot spots" where the localized surface plasmons experience resonant excitation enabling intense enhancements of local electromagnetic fields [80]. Also, the adjacent gold ligaments experience electromagnetic coupling which further leads to improvement in the localized field intensity adding to the overall SERS enhancement [81]. A graph depicting the spectrum with the most intense Raman signals for each bipy concentration can be found in Fig. S6 in the supplementary material. Fig. 6 (b) below displays the average Raman signal for 10 accumulations per bipy concentration after excluding the extraordinarily high signal arising from a possible hotspot encounter (visible in the case of 10^{-15} M bipy concentration in Fig. S6 of the supplementary material). In Fig. 6 (c) the relationship between bipy concentration and the average SERS intensity at 1614 cm^{-1} is demonstrated; variation of degree of intensity at each concentration is represented by the error bars. Considering this average signal intensity and the related errors per bipy concentration there exists a decreasing trend of SERS intensity as a function of the decreasing concentration of the analyte considering the error bars which is in agreement with the literature. The detection limit is as low as 10^{-15} M which is an impressive achievement of this NPG sample. Fig. S7 in the

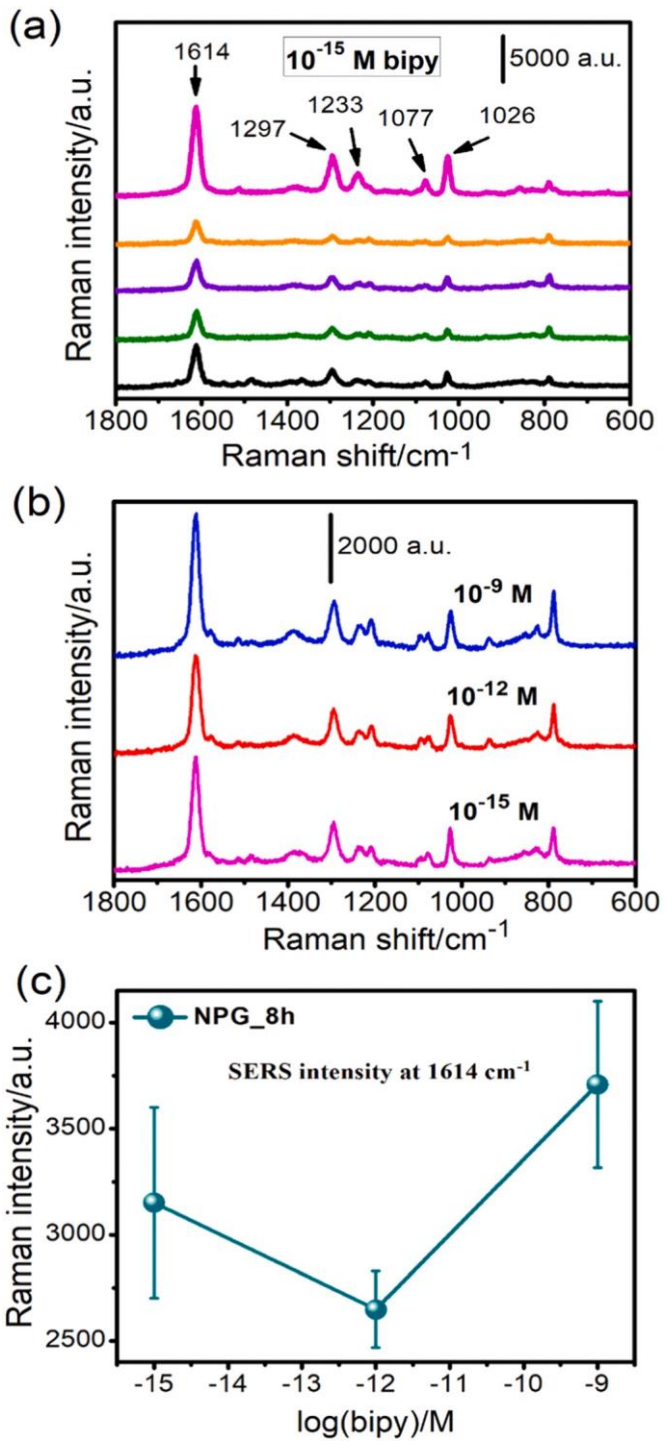

Fig. 6. (a) SERS spectra of bipy at 10^{-15} M concentration at different sites on NPG_8h. (b) SERS spectra of NPG_8h for different bipy concentrations (10 accumulations each). (c) Relationship between the logarithm of bipy concentration and the average SERS intensity at 1614 cm^{-1} and the related error bars.

dealloying $Au_{30}Cu_{38}Ag_7Pd_5Si_{20}$ metallic glass precursor electrochemically [42]; 10^{-12} M for lamellar nanoporous gold thin film [82]; 10^{-14} M for NPGs obtained by chemically dealloying $Au_{30}Cu_{38}Ag_7Pd_5Si_{20}$ amorphous alloy [9] and $Au_{20}Cu_{48}Ag_7Pd_5Si_{20}$ metallic glass precursor [35] respectively. Fig. 7 (a,b) respectively show 3D and 2D maps of SERS intensity at 1614 cm^{-1} with bipy concentration of 10^{-12} M. These mapping images evidently depict the presence of ''hotspots". (For interpretation of the references to colour in this figure legend, the reader is referred to the Web version of this article.)

supplementary material shows the comparison of SERS spectra obtained for 10^{-15} M and further lower concentration of 10^{-16} M; the latter showed no signals concluding that 10^{-15} M is indeed the detection limit. When compared to previously reported NPG samples acting as SERS substrates, the detection limit of 10^{-15} M for bypridine exhibited by our sample is lower than that for a number of samples such as 5×10^{-10} M for NPG of ligament size 5 nm [43]; 10^{-11} M for NPG obtained by

4. Economic and sustainability factors

An important objective of this work has been to synthesize high quality NPG in a cost-effective and sustainable manner. Discussed below are some reasons which make for a convincing case in favour of this NPG sample as a better alternative among contemporary candidates.

(i) Considering the current commodity prices in London Metal Exchange, i.e., the world centre for the trading of industrial metals, it is evident that Fe can be procured quite cheaply [83]. The actual price of Fe falls around 450 $/ton while that of some other common metals used in the production of the precursors for NPG fabrication is as follows: Al about 3000 $/ton (for Al–Au alloy), Cu about 9000 $/ton (for Cu–Au alloy) and Ag is 800 $/kg for Ag–Au alloys (which is about 2000 times higher than Fe). Hence, it serves as a better option in terms of inexpensiveness and availability.

(ii) We have utilized the lowest possible concentration of Au for the precursor, i.e., 33 at. %, in accordance with the parting limit. Since it is rather common to use Au-rich precursors as reported in literature our approach is quite contrary which allows us to cut down the total cost right from the start.

(iii) The usage of multi-metallic crystalline as well as amorphous precursors has been commonly seen in many previously reported articles. Procuring a number of metals for a single precursor (some of them being critical raw materials) only adds to the overall cost. Additionally, this can complicate the synthetic procedures requiring usually more than one dealloying process to remove the multiple less-noble metals. On the other hand, we have employed a bimetallic precursor pairing Fe with Au, knowing well that Fe is a low-cost, hugely abundant and active metal. Such approach has greatly reduced the cost and simplified our synthesis procedure while advocating the issue of sustainability at the same time.

(iv) We have not employed any critical raw material to combine with Au for the precursor alloy. Ag, a critical raw material, is a commonly used Au-pairing metal [84]. Fe, being an active, abundant and cheap metal, has been used to replace Ag giving similar or better outputs in terms of the quality and properties of the resultant NPG.

Based on all the above points the NPG sample reported in this work is an outstanding, cost-effective and sustainable alternative as an electrocatalyst for HER as well as a SERS-active substrate.

5. Conclusions

Nanoporous Gold has been successfully obtained using a cheap and efficient $Au_{33}Fe_{67}$ precursor. The precursor ribbons were prepared by subsequent techniques of arc melting and melt-spinning. Chemical dealloying was carried out in 1 M HNO_3 at 70 °C for different lengths of time. The obtained NPG samples display distinct nanoporous morphology. Few trends are noticeable, i.e., with the increase in the dealloying time, there is an increase in - (i) Au atomic percentage; (ii) the size of the ligaments, and; (iii) the homogeneity of the surface morphology. The sample chemically dealloyed in 1 M HNO_3 at 70 °C for 8 h, i.e., NPG_8h, was selected to be tested for its catalytic activity in HER in 0.5 M H_2SO_4 as it possessed the largest electrochemically active

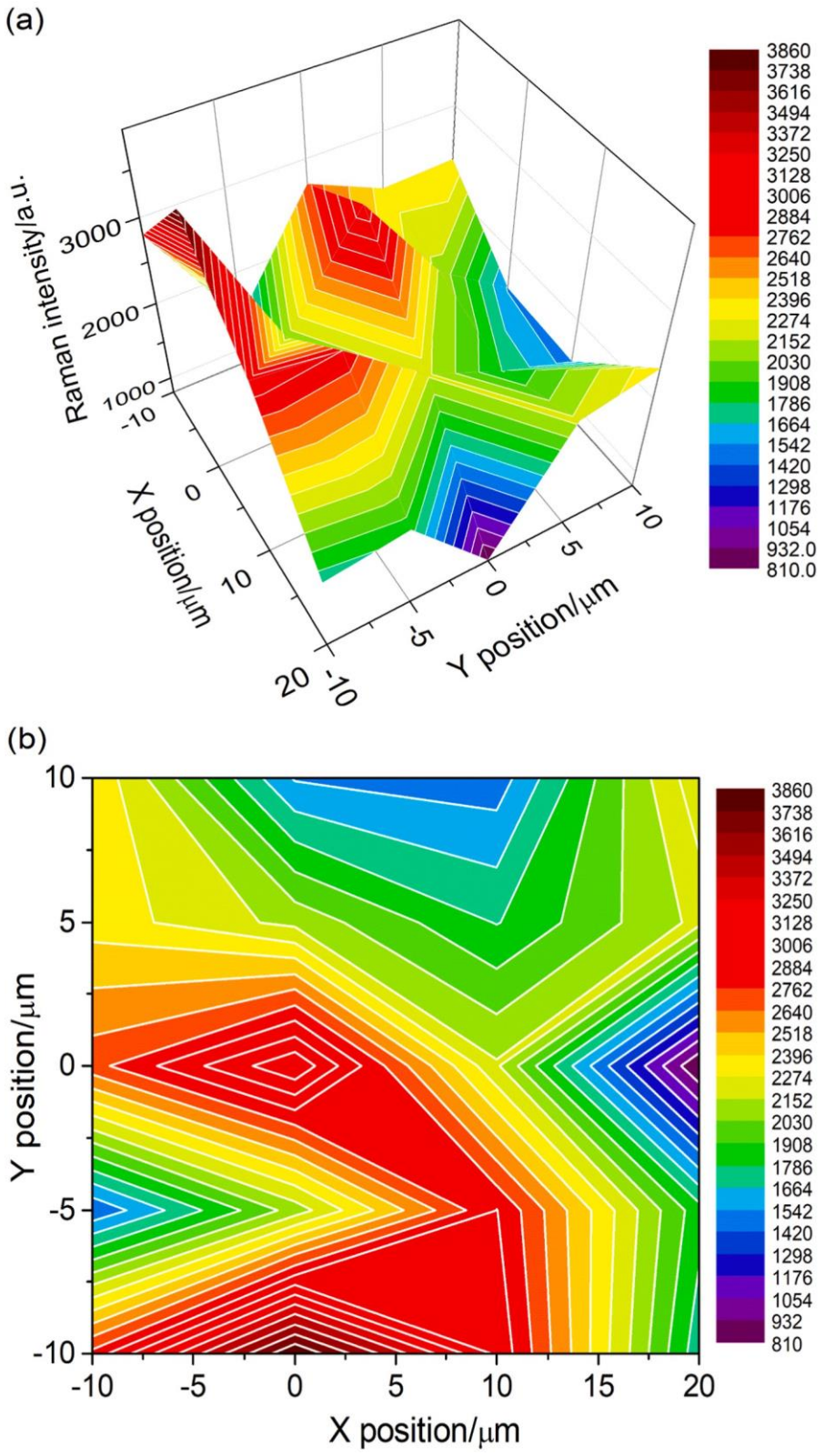

Fig. 7. (a) SERS 3D and (b) 2D surface maps of 20 × 30 μm^2 area at 1614 cm^{-1} for 10^{-12} M bipy.

surface area and thus, the most number of active sites. The sample shows 5 mA cm^{-2} current density at −0.38 V overpotential. The obtained small Tafel slope, low onset potential and high exchange current density, i.e., 47 mV dec^{-1}, -4 mV and 0.12 mA cm^{-2} respectively, and the sample's impressive stability for more than 20 h, evidently indicate that this sample makes for an excellent candidate as a low-cost, easily-synthesized, efficient and durable electrocatalyst for HER. Besides, NPG_8h also exhibited strong SERS potential possessing a low value of 10^{-15} M as the detection limit for 4,4′-bipyridine. The mapping image for SERS intensity with bipy concentration of 10^{-12} M approves the widespread

hot spots. The ligaments experiencing electromagnetic coupling, the localized electromagnetic fields enhanced within and around nano-sized pores and ligaments, and the confined SERS-active atoms can all be attributed for the strong SERS enhancement. Thus, the NPG sample possesses excellent potential in applications related to life science and ultrasensitive instrumentation being an inexpensive and highly sensitive SERS-active substrate.

CRediT authorship contribution statement

Deepti Raj: Conceptualization, Data curation, Formal analysis, Investigation, Methodology, Visualization, Writing – original draft, Writing – review & editing. **Mauro Palumbo:** Data curation. **Gianluca Fiore:** Investigation, Methodology, All authors have read and agreed to the published version of the manuscript. **Federica Celegato:** Investigation. **Federico Scaglione:** Conceptualization, Data curation, Formal analysis, Investigation, Methodology, Supervision, Validation, Visualization, Writing – review & editing, M.B. **Paola Rizzi:** Conceptualization, Formal analysis, Funding acquisition, Project administration, Resources, Supervision, Validation, Visualization, Writing – review & editing.

Declaration of competing interest

The authors declare that they have no known competing financial interests or personal relationships that could have appeared to influence the work reported in this paper.

Data availability

Data will be made available on request.

Acknowledgement

NanoFacility Piemonte, INRIM has to be thanked for the SEM images as well as Compagnia di San Paolo-Bando ex-post-Anno 2018 for the funding.

Appendix A. Supplementary data

Supplementary data to this article can be found online at https://doi.org/10.1016/j.matchemphys.2022.126883.

References

[1] I. McCue, E. Benn, B. Gaskey, J. Erlebacher, Dealloying and dealloyed materials, Annu. Rev. Mater. Res. 46 (2016) 263–286, https://doi.org/10.1146/annurev-matsci-070115-031739.
[2] S.H. Kim, Nanoporous gold: preparation and applications to catalysis and sensors, Curr. Appl. Phys. 18 (2018) 810–818, https://doi.org/10.1016/j.cap.2018.03.021.
[3] Y. Xue, F. Scaglione, F. Celegato, P. Denis, H.-J. Fecht, P. Rizzi, L. Battezzati, Shape controlled gold nanostructures on de-alloyed nanoporous gold with excellent SERS performance, Chem. Phys. Lett. 709 (2018) 46–51, https://doi.org/10.1016/j.cplett.2018.08.044.
[4] F. Scaglione, Y. Xue, F. Celegato, P. Rizzi, L. Battezzati, Amorphous molybdenum sulphide @ nanoporous gold as catalyst for hydrogen evolution reaction in acidic environment, J. Mater. Sci. 53 (2018) 12388–12398, https://doi.org/10.1007/s10853-018-2490-2.
[5] F. Scaglione, A. Gebert, L. Battezzati, Dealloying of an Au-based amorphous alloy, Intermetallics 18 (2010) 2338–2342, https://doi.org/10.1016/j.intermet.2010.08.005.
[6] J. Erlebacher, M.J. Aziz, a Karma, N. Dimitrov, K. Sieradzki, Evolution of nanoporosity in dealloying, Nature 410 (2001) 450–453, https://doi.org/10.1038/35068529.
[7] J. Erlebacher, An atomistic description of dealloying, J. Electrochem. Soc. 151 (2004) C614, https://doi.org/10.1149/1.1784820.
[8] J. Erlebacher, K. Sieradzki, Pattern formation during dealloying, Scripta Mater. 49 (2003) 991–996, https://doi.org/10.1016/S1359-6462(03)00471-8.
[9] Y. Xue, F. Scaglione, P. Rizzi, L. Battezzati, Improving the chemical de-alloying of amorphous Au alloys, Corrosion Sci. 127 (2017) 141–146, https://doi.org/10.1016/j.corsci.2017.08.026.
[10] F. Scaglione, P. Rizzi, F. Celegato, L. Battezzati, Synthesis of nanoporous gold by free corrosion of an amorphous precursor, J. Alloys Compd. 615 (2014) S142–S147, https://doi.org/10.1016/j.jallcom.2014.01.239.
[11] F. Scaglione, F. Celegato, P. Rizzi, L. Battezzati, A comparison of de-alloying crystalline and amorphous multicomponent Au alloys, Intermetallics 66 (2015) 82–87, https://doi.org/10.1016/j.intermet.2015.06.022.
[12] S. Van Petegem, S. Brandstetter, R. Maass, A.M. Hodge, B.S. El-Dasher, J. Biener, B. Schmitt, C. Borca, H. Van Swygenhoven, On the microstructure of nanoporous gold: an X-ray diffraction study, Nano Lett. 9 (2009) 1158–1163, https://doi.org/10.1021/nl803799q.
[13] F. Scaglione, P. Rizzi, L. Battezzati, De-alloying kinetics of an Au-based amorphous alloys, J. Alloys Compd. 536 (2012) S60–S64, https://doi.org/10.1016/j.jallcom.2011.11.087.
[14] P. Rizzi, F. Scaglione, L. Battezzati, Nanoporous gold by dealloying of an amorphous precursor, J. Alloys Compd. 586 (2014) S117–S120, https://doi.org/10.1016/j.jallcom.2012.11.029.
[15] Z. He, Y. Huang, F. He, Preparation of nanoporous molybdenum film by dealloying an immiscible Mo-Zn system for hydrogen evolution reaction, RSC Adv. 6 (2016) 15390–15393, https://doi.org/10.1039/C5RA24426A.
[16] X. Li, Q. Chen, I. McCue, J. Snyder, P. Crozier, J. Erlebacher, K. Sieradzki, Dealloying of noble-metal alloy nanoparticles, Nano Lett. 14 (2014) 2569–2577, https://doi.org/10.1021/nl500377g.
[17] E.M. Paschalidou, G. Fiore, Y. Xue, F. Scaglione, F. Celegato, A. Gebert, S. Oswald, U. Wolff, P. Rizzi, L. Battezzati, Comparing selective corrosion of Au-based amorphous, partially amorphous, and devitrified alloys, J. Alloys Compd. 745 (2018) 212–216, https://doi.org/10.1016/j.jallcom.2018.02.204.
[18] The Materials Information Society, ASM Handbook Volume 3 - Alloy Phase Diagrams, ASM Handb., 1992, https://doi.org/10.1007/BF02869318.
[19] D.T.L. Alexander, D. Forrer, E. Rossi, E. Lidorikis, S. Agnoli, G.D. Bernasconi, J. Butet, O.J.F. Martin, V. Amendola, Electronic structure-dependent surface plasmon resonance in single Au-Fe nanoalloys, Nano Lett. 19 (2019) 5754–5761, https://doi.org/10.1021/acs.nanolett.9b02396.
[20] E. Bosco, P. Rizzi, M. Baricco, Phase transformations in Au-Fe melt spun alloys, Mater. Sci. Eng. 375–377 (2004) 468–472, https://doi.org/10.1016/j.msea.2003.10.048.
[21] E. Bosco, P. Rizzi, M. Baricco, Rapid solidification of immiscible alloys, J. Magn. Magn Mater. 262 (2003) 64–68, https://doi.org/10.1016/S0304-8853(03)00020-9.
[22] M. Baricco, E. Bosco, E. Olivetti, M. Palumbo, P. Rizzi, A. Stantero, L. Battezzati, Rapid solidification of alloys, Int. J. Mater. Prod. Technol. 20 (2004) 358, https://doi.org/10.1504/IJMPT.2004.004762.
[23] J. Zhu, L. Hu, P. Zhao, L.Y.S. Lee, K.-Y. Wong, Recent advances in electrocatalytic hydrogen evolution using nanoparticles, Chem. Rev. 120 (2020) 851–918, https://doi.org/10.1021/acs.chemrev.9b00248.
[24] L.P. Hern´andez-Saravia, A. Sukeri, M. Bertotti, Fabrication of nanoporous gold-islands via hydrogen bubble template: an efficient electrocatalyst for oxygen reduction and hydrogen evolution reactions, Int. J. Hydrogen Energy 44 (2019) 15001–15008, https://doi.org/10.1016/j.ijhydene.2019.04.186.
[25] W. Yan, W. Wu, K. Wang, Z. Tang, S. Chen, Oxygen reduction reaction and hydrogen evolution reaction catalyzed by carbon-supported molybdenum-coated palladium nanocubes, Int. J. Hydrogen Energy 43 (2018) 17132–17141, https://doi.org/10.1016/j.ijhydene.2018.07.097.
[26] G. Darabdhara, M.R. Das, M.A. Amin, G.A.M. Mersal, N.Y. Mostafa, S.S. Abd El-Rehim, S. Szunerits, R. Boukherroub, Au Ni alloy nanoparticles supported on reduced graphene oxide as highly efficient electrocatalysts for hydrogen evolution and oxygen reduction reactions, Int. J. Hydrogen Energy 43 (2018) 1424–1438, https://doi.org/10.1016/j.ijhydene.2017.11.048.
[27] M.K. Kundu, T. Bhowmik, S. Barman, Gold aerogel supported on graphitic carbon nitride: an efficient electrocatalyst for oxygen reduction reaction and hydrogen evolution reaction, J. Mater. Chem. A. 3 (2015) 23120–23135, https://doi.org/10.1039/C5TA06740E.
[28] D. Yan, S. Dou, L. Tao, Z. Liu, Z. Liu, J. Huo, S. Wang, Electropolymerized supermolecule derived N, P co-doped carbon nanofiber networks as a highly efficient metal-free electrocatalyst for the hydrogen evolution reaction, J. Mater. Chem. A. 4 (2016) 13726–13730, https://doi.org/10.1039/C6TA05863A.
[29] X. Fan, Z. Peng, R. Ye, H. Zhou, X. Guo, M3C (M: Fe, Co, Ni) nanocrystals encased in graphene nanoribbons: an active and stable bifunctional electrocatalyst for oxygen reduction and hydrogen evolution reactions, ACS Nano 9 (2015) 7407–7418, https://doi.org/10.1021/acsnano.5b02420.
[30] J. Tian, W. Wu, Z. Tang, Y. Wu, R. Burns, B. Tichnell, Z. Liu, S. Chen, Oxygen reduction reaction and hydrogen evolution reaction catalyzed by Pd-Ru nanoparticles encapsulated in porous carbon nanosheets, Catalysts 8 (2018) 329, https://doi.org/10.3390/catal8080329.
[31] H. Yang, Y. Zhang, F. Hu, Q. Wang, Urchin-like CoP nanocrystals as hydrogen evolution reaction and oxygen reduction reaction dual-electrocatalyst with superior stability, Nano Lett. 15 (2015) 7616–7620, https://doi.org/10.1021/acs.nanolett.5b03446.
[32] X. Ren, F. Yang, R. Chen, P. Ren, Y. Wang, Improvement of HER activity for MoS2: insight into the effect and mechanism of phosphorus post-doping, New J. Chem. 44 (2020) 1493–1499, https://doi.org/10.1039/C9NJ05229A.
[33] A. Sukeri, M. Bertotti, Nanoporous gold surface: an efficient platform for hydrogen evolution reaction at very low overpotential, J. Braz. Chem. Soc. 29 (2018) 226–231, https://doi.org/10.21577/0103-5053.20170132.
[34] Y. Mie, H. Takayama, Y. Hirano, Facile control of surface crystallographic orientation of anodized nanoporous gold catalyst and its application for highly

efficient hydrogen evolution reaction, J. Catal. 389 (2020) 476–482, https://doi.org/10.1016/j.jcat.2020.06.023.
[35] Y. Xue, F. Scaglione, E.M. Paschalidou, P. Rizzi, L. Battezzati, Excellent surface enhanced Raman scattering obtained with nanoporous gold fabricated by chemical de-alloying, Chem. Phys. Lett. 665 (2016) 6–9, https://doi.org/10.1016/j.cplett.2016.10.046.
[36] A. Otto, The 'chemical' (electronic) contribution to surface-enhanced Raman scattering, J. Raman Spectrosc. 36 (2005) 497–509, https://doi.org/10.1002/jrs.1355.
[37] S.-Y. Ding, E.-M. You, Z.-Q. Tian, M. Moskovits, Electromagnetic theories of surface-enhanced Raman spectroscopy, Chem. Soc. Rev. 46 (2017) 4042–4076, https://doi.org/10.1039/C7CS00238F.
[38] E. Massarini, P. Wa¨sterby, L. Landstro¨m, C. Lejon, O. Beck, P.O. Andersson, Methodologies for assessment of limit of detection and limit of identification using surface-enhanced Raman spectroscopy, Sensor. Actuator. B Chem. 207 (2015) 437–446, https://doi.org/10.1016/j.snb.2014.09.116.
[39] N.P.W. Pieczonka, R.F. Aroca, Single molecule analysis by surfaced-enhanced Raman scattering, Chem. Soc. Rev. 37 (2008) 946, https://doi.org/10.1039/b709739p.
[40] L. Zhang, H. Liu, L. Chen, P. Guan, B. Chen, T. Fujita, Y. Yamaguchi, H. Iwasaki, Q.-K. Xue, M. Chen, Large-scale growth of sharp gold nano-cones for single-molecule SERS detection, RSC Adv. 6 (2016) 2882–2887, https://doi.org/10.1039/C5RA22321K.
[41] Y. Jiao, J.D. Ryckman, P.N. Ciesielski, C.A. Escobar, G.K. Jennings, S.M. Weiss, Patterned nanoporous gold as an effective SERS template, Nanotechnology 22 (2011), 295302, https://doi.org/10.1088/0957-4484/22/29/295302.
[42] F. Scaglione, E.M. Paschalidou, P. Rizzi, S. Bordiga, L. Battezzati, Nanoporous gold obtained from a metallic glass precursor used as substrate for surface-enhanced Raman scattering, Phil. Mag. Lett. 95 (2015) 474–482, https://doi.org/10.1080/09500839.2015.1093665.
[43] L.H. Qian, X.Q. Yan, T. Fujita, A. Inoue, M.W. Chen, Surface enhanced Raman scattering of nanoporous gold: smaller pore sizes stronger enhancements, Appl. Phys. Lett. 90 (2007), 153120, https://doi.org/10.1063/1.2722199.
[44] Y. Xue, F. Scaglione, P. Rizzi, L. Battezzati, High performance SERS on nanoporous gold substrates synthesized by chemical de-alloying a Au-based metallic glass, Appl. Surf. Sci. 426 (2017) 1113–1120, https://doi.org/10.1016/j.apsusc.2017.07.302.
[45] S.A.S. Machado, L.A. Avaca, The hydrogen evolution reaction on nickel surfaces stabilized by H-absorption, Electrochim, Acta 39 (1994) 1385–1391, https://doi.org/10.1016/0013-4686(94)E0003-I.
[46] S.H. Ahn, S.J. Hwang, S.J. Yoo, I. Choi, H.-J. Kim, J.H. Jang, S.W. Nam, T.-H. Lim, T. Lim, S.-K. Kim, J.J. Kim, Electrodeposited Ni dendrites with high activity and durability for hydrogen evolution reaction in alkaline water electrolysis, J. Mater. Chem. 22 (2012) 15153–15159, https://doi.org/10.1039/C2JM31439H.
[47] H. Ogihara, M. Fujii, T. Saji, Hydrogen evolution reaction (HER) over electroless-deposited nickel nanospike arrays, RSC Adv. 4 (2014) 58660–58663, https://doi.org/10.1039/C4RA11646A.
[48] H. Lukas, S.G. Fries, B. Sundman, Computational Thermodynamics, Cambridge University Press, Cambridge, 2007, https://doi.org/10.1017/CBO9780511804137.
[49] Thermo-calc software (n.d.), https://thermocalc.com/. (Accessed 14 June 2021).
[50] P.A. Beck, H. Okamoto, T.B. Massalski, L.J. Swartzendruber, Phase Diagrams of Binary Iron Alloys, American Society for Metals, Metals Park, OH, 1993.
[51] D. Favez, J.D. Wagni`ere, M. Rappaz, Au-Fe alloy solidification and solid-state transformations, Acta Mater. 58 (2010) 1016–1025, https://doi.org/10.1016/j.actamat.2009.10.017.
[52] M. Palumbo, L. Battezzati, Thermodynamics and kinetics of metallic amorphous phases in the framework of the CALPHAD approach, Calphad 32 (2008) 295–314, https://doi.org/10.1016/j.calphad.2007.12.002.
[53] P.S.M. Kumar, T. Sivakumar, T. Fujita, R. Jayavel, H. Abe, Synthesis of metastable Au-Fe alloy using ordered nanoporous silica as a hard template, Metals 8 (2018) 1–7, https://doi.org/10.3390/met8010017.
[54] M. Tavakolian, P. Salimi, Z. Zand, M.M. Najafpour, Water oxidation by manganese oxides, in: R. van Eldik, -A. C.D.B.T, I.C. Hubbard (Eds.), Water Oxid. Catal., Academic Press, 2019, pp. 115–150, https://doi.org/10.1016/bs.adioch.2019.03.003.
[55] C. Yang, M.Y. Gao, Q.B. Zhang, J.R. Zeng, X.T. Li, A.P. Abbott, In-situ activation of self-supported 3D hierarchically porous Ni3S2 films grown on nanoporous copper as excellent pH-universal electrocatalysts for hydrogen evolution reaction, Nano Energy 36 (2017) 85–94, https://doi.org/10.1016/j.nanoen.2017.04.032.
[56] L. Yang, Y. Lv, D. Cao, Co,N-codoped nanotube/graphene 1D/2D heterostructure for efficient oxygen reduction and hydrogen evolution reactions, J. Mater. Chem. A. 6 (2018) 3926–3932, https://doi.org/10.1039/C7TA11140A.
[57] N. Prabu, T. Kesavan, G. Maduraiveeran, M. Sasidharan, Bio-derived nanoporous activated carbon sheets as electrocatalyst for enhanced electrochemical water splitting, Int. J. Hydrogen Energy 44 (2019) 19995–20006, https://doi.org/10.1016/j.ijhydene.2019.06.016.
[58] R.D. Nikam, A.-Y. Lu, P.A. Sonawane, U.R. Kumar, K. Yadav, L.-J. Li, Y.-T. Chen, Three-dimensional heterostructures of MoS 2 nanosheets on conducting MoO 2 as an efficient electrocatalyst to enhance hydrogen evolution reaction, ACS Appl. Mater. Interfaces 7 (2015) 23328–23335, https://doi.org/10.1021/acsami.5b07960.
[59] X. Xiao, C. Engelbrekt, M. Zhang, Z. Li, J. Ulstrup, J. Zhang, P. Si, A straight forward approach to electrodeposit tungsten disulfide/poly(3,4-ethylenedioxythiophene) composites onto nanoporous gold for the hydrogen evolution reaction, Appl. Surf. Sci. 410 (2017) 308–314, https://doi.org/10.1016/j.apsusc.2017.03.130.
[60] M. Gong, W. Zhou, M.-C. Tsai, J. Zhou, M. Guan, M.-C. Lin, B. Zhang, Y. Hu, D.-Y. Wang, J. Yang, S.J. Pennycook, B.-J. Hwang, H. Dai, Nanoscale nickel oxide/nickel heterostructures for active hydrogen evolution electrocatalysis, Nat. Commun. 5 (2014) 4695, https://doi.org/10.1038/ncomms5695.
[61] X. Yang, W. Xu, S. Cao, S. Zhu, Y. Liang, Z. Cui, X. Yang, Z. Li, S. Wu, A. Inoue, L. Chen, An amorphous nanoporous PdCuNi-S hybrid electrocatalyst for highly efficient hydrogen production, Appl. Catal. B Environ. 246 (2019) 156–165, https://doi.org/10.1016/j.apcatb.2019.01.030.
[62] Q. Tang, D. Jiang, Mechanism of hydrogen evolution reaction on 1T-MoS2 from first principles, ACS Catal. 6 (2016) 4953–4961, https://doi.org/10.1021/acscatal.6b01211.
[63] A.S. Bin Mohd Najib, M. Iqbal, M.B. Zakaria, S. Shoji, Y. Cho, X. Peng, S. Ueda, A. Hashimoto, T. Fujita, M. Miyauchi, Y. Yamauchi, H. Abe, Active faceted nanoporous ruthenium for electrocatalytic hydrogen evolution, J. Mater. Chem. A. 8 (2020) 19788–19792, https://doi.org/10.1039/D0TA04223D.
[64] J. Zhang, X. Wang, Y. Xue, Z. Xu, J. Pei, Z. Zhuang, Self-assembly precursor-derived MoP supported on N,P-codoped reduced graphene oxides as efficient catalysts for hydrogen evolution reaction, Inorg. Chem. 57 (2018) 13859–13865, https://doi.org/10.1021/acs.inorgchem.8b02359.
[65] X. Xiao, C. Engelbrekt, Z. Li, P. Si, Hydrogen evolution at nanoporous gold/tungsten sulfide composite film and its optimization, Electrochim. Acta 173 (2015) 393–398, https://doi.org/10.1016/j.electacta.2015.05.048.
[66] F. Barbir, F.B.T.-P.E.M.F.C, in: E. Barbir (Ed.), Fuel Cell Electrochemistry, PEM Fuel Cells, Elsevier, Boston, 2013, pp. 33–72, https://doi.org/10.1016/B978-0-12-387710-9.00003-5.
[67] A. Abbaspour, F. Norouz-Sarvestani, High electrocatalytic effect of Au-Pd alloy nanoparticles electrodeposited on microwave assisted sol-gel-derived carbon ceramic electrode for hydrogen evolution reaction, Int. J. Hydrogen Energy 38 (2013) 1883–1891, https://doi.org/10.1016/j.ijhydene.2012.11.096.
[68] T.-H. Lu, C.-J. Chen, M. Basu, C.-G. Ma, R.-S. Liu, The CoTe 2 nanostructure: an efficient and robust catalyst for hydrogen evolution, Chem. Commun. 51 (2015) 17012–17015, https://doi.org/10.1039/C5CC06806A.
[69] W. Li, X. Wang, D. Xiong, L. Liu, Efficient and durable electrochemical hydrogen evolution using cocoon-like MoS2 with preferentially exposed edges, Int. J. Hydrogen Energy 41 (2016) 9344–9354, https://doi.org/10.1016/j.ijhydene.2016.03.209.
[70] L. Chen, S. Yang, K. Qian, W. Wei, C. Sun, J. Xie, In situ growth of N-doped carbon coated CoNi alloy with graphene decoration for enhanced HER performance, J. Energy Chem. 29 (2019) 129–135, https://doi.org/10.1016/j.jechem.2018.03.005.
[71] F.-X. Ma, H. Bin Wu, B.Y. Xia, C.-Y. Xu, X.W.D. Lou, Hierarchical β-Mo 2 C nanotubes organized by ultrathin nanosheets as a highly efficient electrocatalyst for hydrogen production, Angew. Chem. Int. Ed. 54 (2015) 15395–15399, https://doi.org/10.1002/anie.201508715.
[72] B. Pierozynski, Hydrogen evolution reaction at Pd-modified carbon fibre and nickel-coated carbon fibre materials, Int. J. Hydrogen Energy 38 (2013) 7733–7740, https://doi.org/10.1016/j.ijhydene.2013.04.092.
[73] B. Pierozynski, T. Mikolajczyk, M. Turemko, E. Czerwosz, M. Kozlowski, Hydrogen evolution reaction at Pd-modified carbon fibre in 0.1 M NaOH, Int. J. Hydrogen Energy 40 (2015) 1795–1799, https://doi.org/10.1016/j.ijhydene.2014.12.029.
[74] J. van der Zalm, S. Chen, W. Huang, A. Chen, Review-recent advances in the development of nanoporous Au for sensing applications, J. Electrochem. Soc. 167 (2020), 037532, https://doi.org/10.1149/1945-7111/ab64c0.
[75] J.M. Gonçalves, A. Kumar, M.I. da Silva, H.E. Toma, P.R. Martins, K. Araki, M. Bertotti, L. Angnes, Nanoporous gold-based materials for electrochemical energy storage and conversion, Energy Technol. 9 (2021), 2000927, https://doi.org/10.1002/ente.202000927.
[76] A. Wittstock, A. Wichmann, J. Biener, M. B¨aumer, Nanoporous gold: a new gold catalyst with tunable properties, Faraday Discuss 152 (2011) 87, https://doi.org/10.1039/c1fd00022e.
[77] Y. Cao, J. Zhang, Y. Yang, Z. Huang, N.V. Long, C. Fu, Engineering of SERS substrates based on noble metal nanomaterials for chemical and biomedical applications, Appl. Spectrosc. Rev. 50 (2015) 499–525, https://doi.org/10.1080/05704928.2014.923901.
[78] M. Moskovits, Surface-enhanced spectroscopy, Rev. Mod. Phys. 57 (1985) 783–826, https://doi.org/10.1103/RevModPhys.57.783.
[79] S.O. Kucheyev, J.R. Hayes, J. Biener, T. Huser, C.E. Talley, A.V. Hamza, Surface-enhanced Raman scattering on nanoporous Au, Appl. Phys. Lett. 89 (2006), 053102, https://doi.org/10.1063/1.2260828.
[80] V. Amendola, S. Scaramuzza, L. Litti, M. Meneghetti, G. Zuccolotto, A. Rosato, E. Nicolato, P. Marzola, G. Fracasso, C. Anselmi, M. Pinto, M. Colombatti, Magneto-plasmonic Au-Fe alloy nanoparticles designed for multimodal SERS-MRI-CT imaging, Small 10 (2014) 2476–2486, https://doi.org/10.1002/smll.201303372.
[81] X.Y. Lang, P.F. Guan, L. Zhang, T. Fujita, M.W. Chen, Characteristic length and temperature dependence of surface enhanced Raman scattering of nanoporous gold, J. Phys. Chem. C 113 (2009) 10956–10961, https://doi.org/10.1021/jp903137n.
[82] A. Chauvin, M. Lafuente, J.Y. Mevellec, R. Mallada, B. Humbert, M.P. Pina, P.-Y. Tessier, A. El Mel, Lamellar nanoporous gold thin films with tunable porosity for

ultrasensitive SERS detection in liquid and gas phase, Nanoscale 12 (2020) 12602–12612, https://doi.org/10.1039/D0NR01721C.
[83] The LONDON METAL EXCHANGE The world centre for industrial metals trading, (n.d.). https://www.lme.com/.
[84] G.A. Blengini, C.E.L. Latunussa, U. Eynard, C. Torres de Matos, D. Wittmer, K. Georgitzikis, C. Pavel, S. Carrara, L. Mancini, M. Unguru, D. Blagoeva, F. Mathieux, D. Pennington, Study on the EU's list of critical raw materials (2020) final report. https://doi.org/10.2873/904613, 2020.